# Excitonic spectra of asymmetric, coupled double quantum wells in electric fields

Johnson Lee, M. O. Vassell, Emil S. Koteles, and B. Elman
*GTE Laboratories Incorporated, 40 Sylvan Road, Waltham, Massachusetts 02254*
(Received 17 October 1988)

The excitonic spectra of asymmetric, coupled double quantum wells in external electric fields were analyzed by a two-band model in the effective-mass envelope-function approximation. Only bound states exist because we assumed that the potential profile has an infinite potential energy at both ends of the double-quantum-well structure. The absorption spectra were calculated in the dipole approximation for the excitonic and the continuum contributions. The variations of the envelope functions, the eigenenergies, the oscillator strengths, and the absorption spectra with electric fields for symmetric and asymmetric wells are presented. We found that, without fields, the asymmetry of the double-quantum-well structures can yield nonzero oscillator strengths for forbidden transitions, but these are too weak to be important in the absorption spectra. With increasing fields, asymmetries of the well structures can yield entirely different spectra depending on the shifts of the central barrier towards the right side or the left side of the well. Theoretical and experimental results were compared and good agreement was reached.

## I. INTRODUCTION

In their most general sense, excitons are elementary crystal excitations produced when a crystal strongly absorbs light of a given photon energy which creates Coulomb coupled electron-hole pairs. The effect of an electrical field on excitons in semiconductors[1] has been studied thoroughly and has been widely used in many electro-optic devices.[2,3] The Franz-Keldysh effect states that, at a given photon energy, the absorption coefficient of the interband transitions increases with electric field.[1] This can be interpreted as a shift of the absorption edge to lower photon energies. When the Coulomb interaction is taken into account, the direct consequences are a broadening of the exciton-absorption line and a shift of the exciton resonance to lower photon energies as the field increases.[1,4,5] This broadening occurs because the electric field lowers the lip of the Coulomb potential energy and concentrates the wave function on the lip side of the Coulomb potential. Consequently, the probability of the electron escaping from the hole (field ionization) increases.[1,4] In short, asymmetry of the effective potential (Coulomb potential plus electric potential) has a great influence on optical-absorption spectra.

Recently, a great deal of attention has been focused on investigations of the electroabsorption in $GaAs/Al_xGa_{1-x}As$ quantum wells (QW's) because of the possibility of designing new types of high-speed electro-optic modulators.[6–8] Upon the application of electric fields (no matter how small) to wells with infinitely thick barriers, the system strictly has no bound states simply because one of the conduction band edges in the barrier regions is lowered to $-\infty$ by the field, i.e., the potential becomes open.[9–10] Therefore, discrete energy levels become continua. However, if the fields are not excessively large, we can treat the particle as quasibound in an effective region, and perform the calculation variationally[9,10] or by perturbation.[11] Alternatively, the exact solution of the effective-mass Schrödinger equation can be obtained by using the resonance-tunneling technique and yields a continuous energy spectrum.[12,13] The optical-absorption spectra as a function of field have been reported[14] for a variational method with the valence-band mixing taken into account. These studies focused on single quantum wells and show that (1) exciton resonances persist even at room temperature; (2) when an electric field is applied perpendicular to a QW large shifts in the optical absorption to lower (red shift) or higher (blue shift) photon energies remain well resolved with little broadening; (3) the intensities at the exciton-resonance energies decrease (increase) for allowed (forbidden) transitions as field increases. All these features are quite different from the effects seen in the bulk semiconductor, GaAs.

The band-gap engineering of quantum-confined systems offers more complex structures, such as the coupled, double quantum well (CDQW),[15–20] which permits flexibility in the study of the Stark effect on excitons and can enhance the performance of electro-optic devices. This structure consists of a pair of QW's separated by a barrier thin enough that particles can interchange between wells by tunneling through the barrier region. Variations of exciton resonance energies with electric fields have been investigated theoretically using the tunneling resonance technique[15,19] and the perturbation method.[18] Usually in experiments, samples are fabricated in CDQW *p-i-n* structures so that bias voltages can be applied. However, in theoretical treatments, the effect of electric fields is calculated. Thus, when theoretical and experimental results are compared, a suitable relation between field and bias voltage must be assumed.

This study was undertaken to ascertain the degree to which structural asymmetries inadvertently introduced into coupled pairs of QW's during growth would affect optical properties. The model developed here permits us to calculate the absorption spectrum of asymmetric CDQW's (i.e., two coupled wells of different thicknesses)

 

as a function of electric field. In our model, we assume that the potential energies at the interfaces of *p-i* and *n-i* of the CDQW *p-i-n* structures are infinite. This assumption ensures the existence of only bound states in the system with electric fields. Confined excitons are described by using the effective-mass approximation in the two-band model. In Sec. II, we present our theoretical model for calculating the eigenenergies and the corresponding envelope functions, and then discuss the excitonic and continuum contributions to the absorption coefficient. In Sec. III, numerical results and experimental data are compared. The influences of the spatial asymmetry of the CDQW with and without fields are discussed in detail. Finally, a summary is presented. In the Appendix numerical schemes for solving the Schrödinger equation are discussed.

## II. THEORY: TWO-BAND MODEL

In our theoretical model, we consider an asymmetric CDQW to have finite depth ($V_e$ in the conduction band and $V_h$ in the valence band) and to experience an external electric field $F$ along the $z$ axis as shown in Fig. 1. Here, $E_g$ is the band-gap energy, $D_1$, $D_2$, and $B$ are the barrier thicknesses, and $W_1$ and $W_2$ are the well thicknesses. The quantity $\delta$, defined as $(W_1-W_2)/2$, indicates the degree of the spatial asymmetry of the CDQW structure. The point $O''$ is at the center of $\overline{AB}$. A confined exciton is then described by using the effective-mass envelope-function approximation. Throughout this section, we adopt atomic units, $\mathcal{R}=m_0e^4/2\hbar^2$ for the energy unit, and $a_B=\hbar^2/m_0e^2$ for the length unit, where $m_0$ is the free-electron mass. The total Hamiltonian for the system is given by

$$H=H_e+H_h+H_{\rm ex} , \tag{1}$$

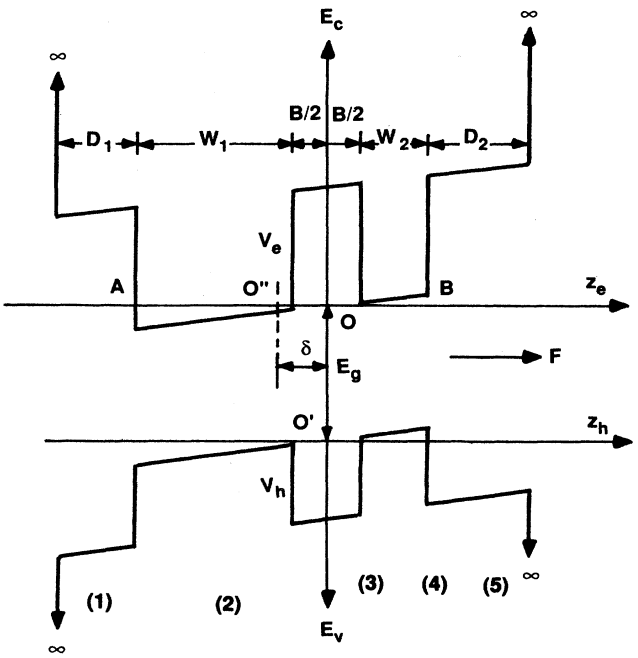


FIG. 1. The potential profile of the CDQW structures.

where

$$H_e=-\partial_{z_e}\frac{1}{m_e^*(z_e)}\partial_{z_e}+V_e(z_e)+Fz_e , \tag{2}$$

$$H_h=-\partial_{z_h}\frac{1}{m_h^*(z_h)}\partial_{z_h}+V_h(z_h)-Fz_h , \tag{3}$$

and

$$H_{\rm ex}=-\frac{1}{\mu}\nabla_\rho^2-(2/\kappa)[\rho^2+(z_e-z_h)^2]^{1/2} \tag{4}$$

$$m_{e,h}^*(z_{e,h})=\begin{cases} m_{e,h}^* & \text{inside the wells} , \\ m_{e,h}^{*\prime} & \text{outside the wells} , \end{cases}$$

and

$$V_{e,h}(z_{e,h})=\begin{cases} 0 & \text{inside the wells} \\ V_{e,h} & \text{outside the wells} \\ \infty & \text{if } z_{e,h}=B/2+(W_2+D_2) \\ & \text{or } (-B/2-W_1-D_1) . \end{cases} \tag{5}$$

Here, $m_e^*$, $m_h^*$, and $\mu$ are the electron effective mass, the hole (heavy or light) effective mass, and the reduced mass, respectively, $F$ is the applied electric field, $\kappa$ is the dielectric constant, and $\rho$ is the relative displacement of the electron and hole in the $x$-$y$ plane. $H_e$ and $H_h$ are used to describe the electron and hole motion in the $z$ direction, respectively, and $H_{\rm ex}$ is employed to depict the excitonic effect via the Coulomb interaction.

We attempt to solve the eigenvalue problems of Eqs. (2)–(4) separately. Firstly, let us consider Eq. (2) for the electron. The envelope functions $f_n(z_e)$ for the electron satisfy

$$H_e f_n(z_e)=E_{cn}f_n(z_e),\ n=1,2,3,\ldots \tag{6}$$

where $E_{cn}$, the eigenenergy, is measured from the reference point $O$ as indicated in Fig. 1. Because the potential energy $V_e(z_e)$ is assumed to be infinite at both ends [see Eq. (5)], the appropriate boundary conditions for $f_n(z_e)$ are

$$f_n(z_e=B/2+W_2+D_2)=f_n(z_e=-B/2-W_1-D_1)=0 . \tag{7}$$

The discrete eigenenergies $E_{cn}$ and the corresponding eigenfunctions $f_n(z_e)$ which satisfy Eq. (5) and boundary conditions [Eq. (6)] can be solved numerically as accurately as desired by using the Runge-Kutta method. This numerical scheme is discussed briefly in the Appendix. An identical numerical procedure can be applied directly to calculate the eigenenergies $E_{vm}$ and the corresponding eigenfunctions $g_m(z_h)$ for the hole. From Eq. (3), we write

$$H_h g_m(z_h)=E_{vm}g_m(z_h) , \tag{8}$$

with the boundary conditions

$$g_m(z_h=B/2+W_2+D_2)=g_m(z_h=-B/2-W_1-D_1)=0 . \tag{9}$$

Here, $E_{vm}$ is measured from the reference point $O'$ as shown in Fig. 1. Once $E_{cn}$ and $f_n(z_e)$ for electron and $E_{vm}$ and $g_m(z_h)$ are determined, Eqs. (1) and (4) give

$$\frac{1}{\mu}\nabla_\rho^2\phi_{nm}(\boldsymbol{\rho})-\left[\frac{2}{\kappa}\int_{-\infty}^{\infty}dz_e\,f_n^2(z_e)\int_{-\infty}^{\infty}dz_h\,g_m^2(z_h)[\rho^2+(z_e-z_h)^2]^{-1/2}\right]\phi_{nm}(\boldsymbol{\rho})=E_{\rm ex}\phi_{nm}(\boldsymbol{\rho})\ , \tag{10}$$

where $\phi_{nm}(\boldsymbol{\rho})$ is the envelope function for the exciton and $E_{\rm ex}$ is the corresponding eigenenergy. The boundary conditions are $\phi_{nm}(\pm\infty)=0$. The total energy $E_{nm}$ (apart from the bulk energy gap $E_g$) and the total envelope function $\psi_{nm}$ of the system with an electron in the $n$th state and a hole in the $m$th state are

$$E_{nm}=E_{cn}+E_{vm}+E_{\rm ex} \tag{11}$$

and

$$\psi_{nm}(\rho,z_e,z_h)=f_n(z_e)g_m(z_h)\phi_{nm}(\rho)\ .$$

It is important to note that, since any information about the electric field $F$ is implicitly contained in the functions $f_n$ and $g_m$, Eq. (10) has an implicit electric-field dependence.[21]

Examination shows that Eq. (10) is difficult to solve, either numerically or analytically, without further approximations. For simplicity, we may approximate Eq. (10) by

$$\frac{1}{\mu}\nabla_\rho^2\phi_{nm}(\boldsymbol{\rho})-\left[\frac{2}{\kappa}(\rho^2+A_{nm}^2)^{-1/2}\right]\phi_{nm}(\boldsymbol{\rho})=E_{\rm ex}\phi_{nm}(\boldsymbol{\rho})\ , \tag{12}$$

where

$$A_{nm}^2=\int_{-\infty}^{\infty}dz_e\,f_n^2(z_e)\int_{-\infty}^{\infty}dz_h\,g_m^2(z_h)(z_e-z_h)^2\ . \tag{13}$$

In this approximation, all information about $F$ is implicitly included in $A_{nm}^2$ through functions $f_n$ and $g_m$. For the exciton energy of the ground state, $E_{\rm ex}=E_b<0$, we adopt a variational method to approximate $E_b$ by choosing the normalized trial wave function

$$\phi_{nm}(\rho)=\left[\frac{\beta^2 e^{\beta A_{nm}}}{2\pi(1+\beta A_{nm})}\right]^{1/2}\times\exp\left[\frac{-\beta(\rho^2+A_{nm}^2)^{1/2}}{2}\right]\ , \tag{14}$$

where $\beta$ is the variational parameter. By using Eq. (14), the expectation value of $E_{\rm ex}$ in Eq. (12) is given by

$$\mu\langle E_b\rangle=\frac{\beta^2}{4}-\frac{\beta^2\eta^2E_1(\eta)}{4(1+\eta)}-\frac{2\mu}{\kappa}\left[\frac{\beta}{1+\eta}\right]\ , \tag{15}$$

where $E_1(\eta)$ is the exponential integral with $\eta=\beta A_{nm}$. After minimization of $\langle E_b\rangle$ with respect to $\beta$, we obtain the exciton binding energy in the $1s$ state and the approximated $\phi_{nm}(\rho)$. The physical quantity needed for later discussions of the absorption coefficient is

$$|\phi_{nm}(0)|^2=\beta^2/2\pi(1+\beta A_{nm})\ . \tag{16}$$

For the exciton energy in the continuum ($E_{\rm ex}\geq 0$), we neglect the $A_{nm}$ term in Eq. (12), and $|\phi_{nm}(0)|^2$ is given by[22]

$$|\phi_{nm}(0)|^2=\frac{2}{1+\exp[-2\pi(\mu/\kappa^2E_{\rm ex})^{1/2}]}=|\phi_{nm}^c(0)|^2\ . \tag{17}$$

The absorption coefficient for radiation of angular frequency $\omega$ propagating along the $z$ axis of the system is calculated by employing the dipole approximation[23] to obtain

$$\alpha^{\rm ex}(\omega)=\frac{c}{\omega}\sum_{n,m,\nu}[P^2I_{nm}^2|\phi_{nm}(0)|^2\delta(E_{nm}^0+E_b-\hbar\omega)]_\nu \tag{18}$$

for the excitonic contribution, and

$$\alpha^{\rm con}(\omega)=\frac{c}{\omega}\sum_{n,m,\nu,\mathbf{k}}\left[P^2I_{nm}^2|\phi_{nm}^c(0)|^2\times\delta\left[\frac{k^2}{\mu}+E_{nm}^0-\hbar\omega\right]\right]_\nu \tag{19}$$

for the continuum contribution, with the overlap integral

$$I_{nm}=\int_{-\infty}^{\infty}dz_e\int_{-\infty}^{\infty}dz_h\,f_n(z_e)g_m(z_h)\delta(z_e-z_h)$$

and

$$E_{nm}^0=E_{nm}+E_g\ , \tag{20}$$

where $P$ is the momentum matrix element and the subindex $\nu$ is used to distinguish the heavy hole (H) or light hole (L) in the valence band. In order to include the effects of spectrum line broadening, we replace the $\delta$ function in Eqs. (18) and (19) by a Lorentzian function of half-width $\Gamma$:

$$\delta(x)\rightarrow\Gamma[\pi(x^2+\Gamma^2)]^{-1} \tag{21}$$

and then perform the integration over $\mathbf{k}$ in Eq. (19). The total absorption coefficient $\alpha$ is

$$\alpha(\omega)=\alpha^{\rm ex}(\omega)+\alpha^{\rm con}(\omega)\ . \tag{22}$$

Note that when we perform the sum over $\nu$ for the heavy hole and the light hole in Eqs. (18) and (19), the relation of $(P^2)_{\rm H}/(P^2)_{\rm L}=\frac{3}{1}$ is incorporated. The oscillator strength for the heavy-hole exciton and the light-hole exciton is defined as

$$(O_{nm})_\nu=C'[P^2I_{nm}^2|\phi_{nm}(0)|^2]_\nu,\quad \nu={\rm H,\ L}\ , \tag{23}$$

where $C'$ is proportionality constant. Conventionally, we categorize optical transitions into two classes: (1) if $n=m$ the transitions are allowed, and (2) if $n\neq m$, the transitions forbidden. However, when an electric field is applied to quantum wells, the potential profile becomes asymmetric, and allowed transitions may weaken and forbidden transitions may become observable. Finally, from the $E_{nm}^0$ and $E_b$ assigned in Eqs. (20) and (15), we define the calculated energies

$$E_{nm}^{\rm tot}=E_{nm}^{0}+E_b\ , \tag{24}$$

which we directly compare to experimental data.

## III. NUMERICAL RESULTS AND DISCUSSION

In order to perform numerical calculations using the model developed in Sec. II, we need to specify the structure parameters: $V_e$, $V_h$, $D_1$, $D_2$, $W_1$, $W_2$, $B$, $m_h^*$ (L and H), and $m_e^*$, for a CDQW. The photoluminescence excitation spectra of a CDQW under various bias voltages, reported in Ref. 20, were originally assigned the following structural parameters: $Ga_{1-x}Al_xAs/GaAs$ with $x=0.27$, $V_e=237.2$ meV, $V_h=101.7$ meV, $D_1=D_2=850$ Å, $W_1=75$ Å$+\delta$, $W_2=75$ Å$-\delta$, $B=18$ Å, $m_e^*=0.067$, $m_{\rm H}^*=0.377$, and $m_{\rm L}^*=0.087$ for the masses in the well regions, and $m_e^*=0.089$, $m_{\rm H'}^*=0.4$, and $m_{\rm L'}^*=0.107$ for the masses in the barrier regions. The common parameters are $\kappa=12.2$ for the dielectric constant and $E_g=1519$ meV for the energy gap of bulk GaAs. This CDQW is spatially symmetric if $\delta=0$. We use this set of data as our input for the numerical calculations, and the results are discussed below. In this section, we assign the notation $nm$H ($nm$L) to represent the transitions between the electron in the $n$th state and the heavy (light) hole in the $m$th state.

### A. Without electric field, $F=0$

First, we investigate the simplest case, i.e., when the system is electric-field free. A typical CDQW with $\delta<0$, i.e., $W_1$ (left well) decreasing but $W_2$ (right well) increasing with increasing $|\delta|$ with $B$ and $AB$ fixed is indicated in Fig. 1. The envelope functions for various $\delta$'s with $0\le-\delta\le60$ Å are plotted in Fig. 2 for the heavy hole. Figure 2(a) shows the envelope functions for the heavy hole in the ground state, i.e., $g_{m=1}(z_h)$, while Fig. 2(b) gives the envelope functions for the heavy hole in the first excited state, $g_{m=2}(z_h)$. When $|\delta|=0$, $g_1$ ($g_2$) has spatial symmetry (antisymmetry) with respect to $z_h$ as expected, because the potential profile has spatial symmetry. When $|\delta|$ increases, $W_1$ ($W_2$) for the left (right) well decreases (increases); thus, the probability of finding a hole in the left (right) well decreases (increases), and $g_1(z_h)$ becomes asymmetric in $z_h$, as shown in Fig. 2(a). When $|\delta|$ is larger than 15 Å or so, $g_1$ is nearly zero in the left-well region. Thus, the CDQW behaves like a single well and $g_1$ becomes almost symmetric in $z_h$. In contrast, the results for the first-excited state are quite different. As indicated in Fig. 2(b), when $|\delta|$ increases, the probability of finding a hole in the left (right) well increases (decreases). However, when $|\delta|$ is larger than 40 Å or so, $g_2(z_h)$ becomes almost antisymmetric because now the CDQW behaves like a single quantum well. Similar conclusions are reached for the envelope functions of electron, $f_n(z_e)$, and light hole.

The oscillator strengths, $O_{nm{\rm H}(nm{\rm L})}$, are shown in Figs. 3(a) and 3(b) as functions of $|\delta|$ for the allowed and forbidden transitions, respectively. For the allowed transitions [Fig. 3(a)], we see that the oscillator strengths have oscillatory behavior as $|\delta|$ increases. When $|\delta|\to0$, we have $O_{22{\rm H}}>O_{11{\rm L}}$, while when $|\delta|\to60$ Å, i.e., the left well almost disappears, we have $O_{22{\rm H}}<O_{11{\rm L}}$. For forbidden transitions [Fig. 3(b)], when $|\delta|\to0$, $O_{nm{\rm H}(nm{\rm L})}\to0$ because the double quantum well has spatial symmetry which yields antisymmetric integrands of $g_m f_n$ in Eq. (20). As $|\delta|$ increases, oscillator strengths first increase and then decrease to zero when $|\delta|\to60$ Å. Here, the CDQW behaves like a single well which has spatial symmetry and yields antisymmetric integrands. As well, Figs. 3(c) and 3(d) show the total energy $E_{nm{\rm H}(nm{\rm L})}^{\rm tot}$ [as defined in Eq. (24)] as a function of $|\delta|$ for the allowed and forbidden transitions, respectively. For the allowed transitions, as $|\delta|$ increases, $E_{11{\rm H}}^{\rm tot}$ and $E_{11{\rm L}}^{\rm tot}$ decrease monotonically while $E_{22{\rm H}}^{\rm tot}$ and $E_{22{\rm L}}^{\rm tot}$ increase to maximum values and then decrease.

The absorption coefficient $\alpha(\hbar\omega)$ for various $|\delta|$ is shown in Fig. 4. In the optical energy range of interest, we see only four peaks, which are identified as allowed transitions. The forbidden transitions do not show up in the absorption spectra because the oscillator strengths

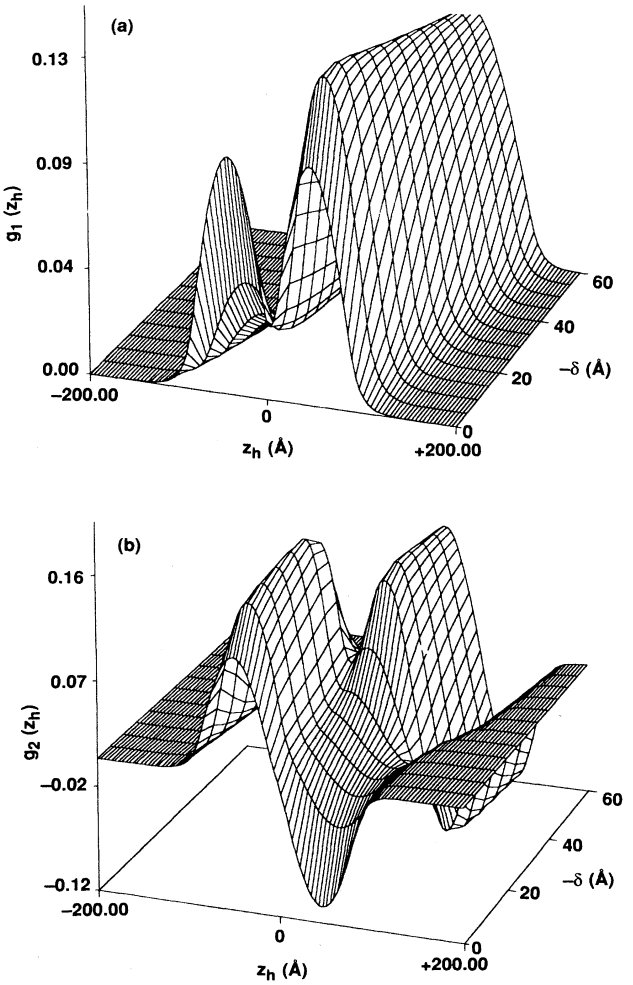


FIG. 2. Three-dimensional plots of the envelope function as functions of $z_h$ and $\delta$ without electric field for the heavy hole in (a) the ground state and (b) the first-excited state.

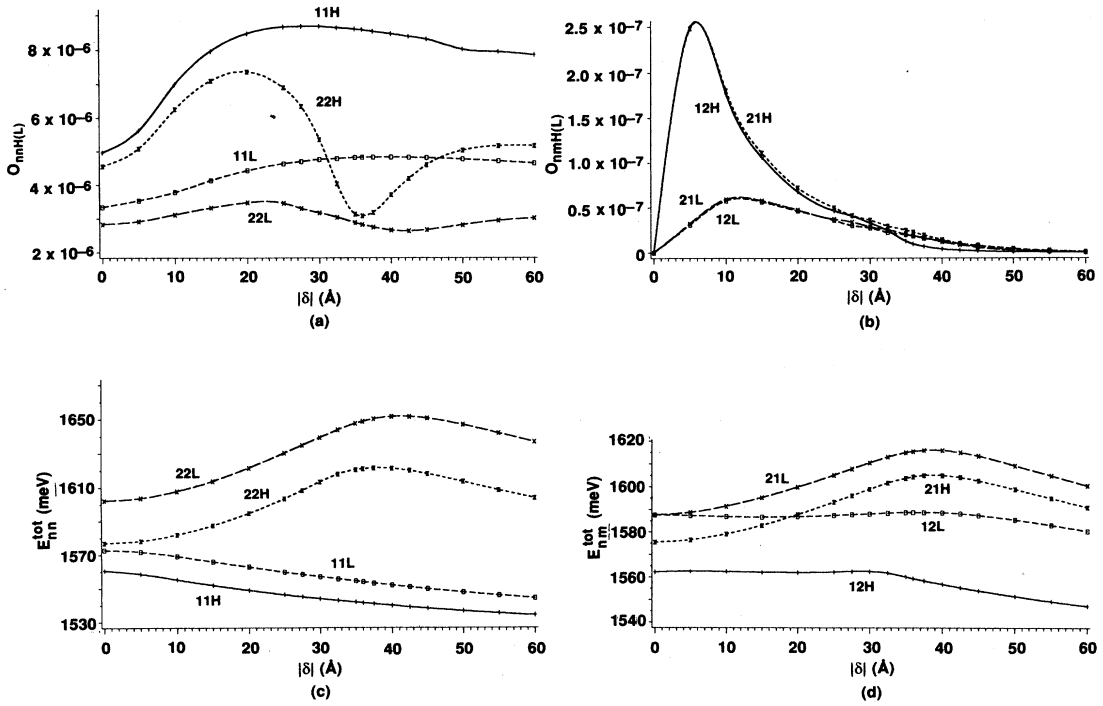


FIG. 3. Without fields, the oscillator strengths and the total energies are plotted as a function of δ for allowed transitions (a) and (c) and for forbidden transitions (b) and (d), respectively.

are one order of magnitude weaker than the oscillator strengths for the allowed transitions for any value of δ, as shown in Figs. 3(a) and 3(b). Here, we notice that when $|\delta|$ increases the 11H and 11L peaks shift toward lower energies, while the 22H and 22L peaks shift toward higher energies, and then move backward to lower energies. These conclusions are reflected exactly in Fig. 3(c). The 11H and 22H peaks (11L and 22L peaks) indicate stronger (weaker) absorptions mainly because the oscillator strengths for the heavy (light) hole are stronger (weaker), as shown in Fig. 3(a). Here, we conclude that without electric fields, even if we make the CDQW asymmetric ($\delta \neq 0$), the oscillator strengths for the forbidden transitions are nonzero but too weak to be clearly observable in the absorption spectra.

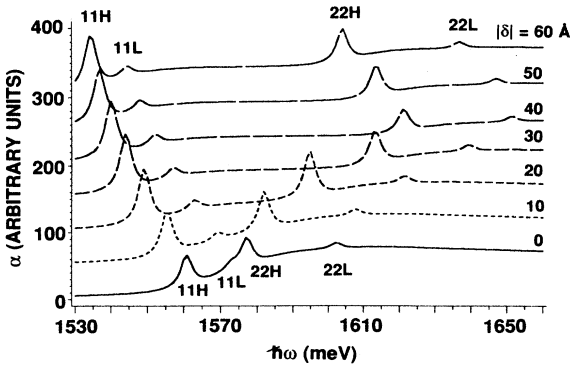


FIG. 4. The absorption spectra of a CDQW for various δ's with zero field.

### B. Symmetric wells with electrical fields ($\delta = 0$, $F \neq 0$)

Even when the structures of the CDQW's are symmetric ($\delta = 0$), the potential profiles becomes asymmetric with respect to the center $O$ of the barrier if an external electric field $F$ is applied as shown in Fig. 5 for the conduction-band edge. The envelope functions for various $F$'s in the ground state (the first-excited state) are shown in Figs. 6(a) [6(d)], and 6(b) [6(e)], and 6(c) [6(f)] for electrons, heavy holes, and light holes, respectively. For the electron in the ground state, Fig. 6(a) indicates that (1) when the field $F$ is zero, $f_1(z_e)$ has spatial symmetry;

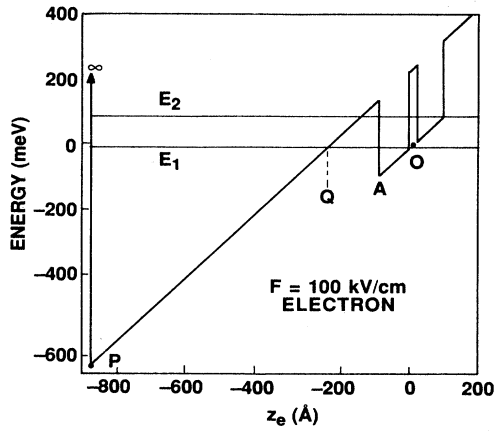


FIG. 5. The potential profile of the conduction-band edge of the CDQW with $F = 100$ kV/cm is plotted. $E_1$ ($E_2$) represents the electron in the ground (first-excited) state.

(2) when $F=50$ kV/cm, the probability of finding an electron in the left (right) well increases (decreases); and (3) when $F=100$ kV/cm, almost all electrons are in the left well and some of the electrons begin to penetrate through the barrier located at point $A$ of Fig. 5 and to reside in the left-barrier region. The penetrating part of the envelope function in the left-barrier region is oscillatory with a decreasing amplitude as $z_e$ reaches the point $P$ of Fig. 5. Because the electric field strongly tilts the potential profile such that the effective barrier width $QA$ is reduced and the point $P$ is very low, as shown in Fig. 5, the left-barrier region becomes a triangular well (no longer a barrier) containing those escaped electrons. The penetration phenomena become even more evident for the cases of the heavy hole and the light hole as shown in Fig. 6(b) and 6(c), respectively. The penetration for the holes (L and H) is enhanced because the potential barrier $V_h$ is smaller than the potential barrier $V_e$. Since holes carry positive charges, the probability of finding a hole in the right (left) well increases (decreases) when $F\neq 0$, and some of the holes reside in the right-barrier region after penetrating through the barrier. Relative to the bottom of the right well, $|E_{1H}|$ is less than $|E_{1L}|$ because $m_L^*$ is less than $m_H^*$; thus, the envelope function for the light hole has stronger oscillations in the right barrier region. For the first-excited states, shown in Figs. 6(d), 6(e), and 6(f) for the electron, the heavy hole, and light hole, respectively, conclusions are obtained which are similar to those discussed for the ground state [Figs. 5(a)–5(c)], except for the population distribution of electrons. For the electron in the first-excited state, $f_2(z_e)$, Fig. 6(d) shows that when $F$ increases, the probability of finding an electron in the right well increases [instead of decreasing as discussed for the envelope functions in Fig. 6(a)] and then slightly decreases. Compared with the ground state, the leaking of the particles out of the wells is stronger for the

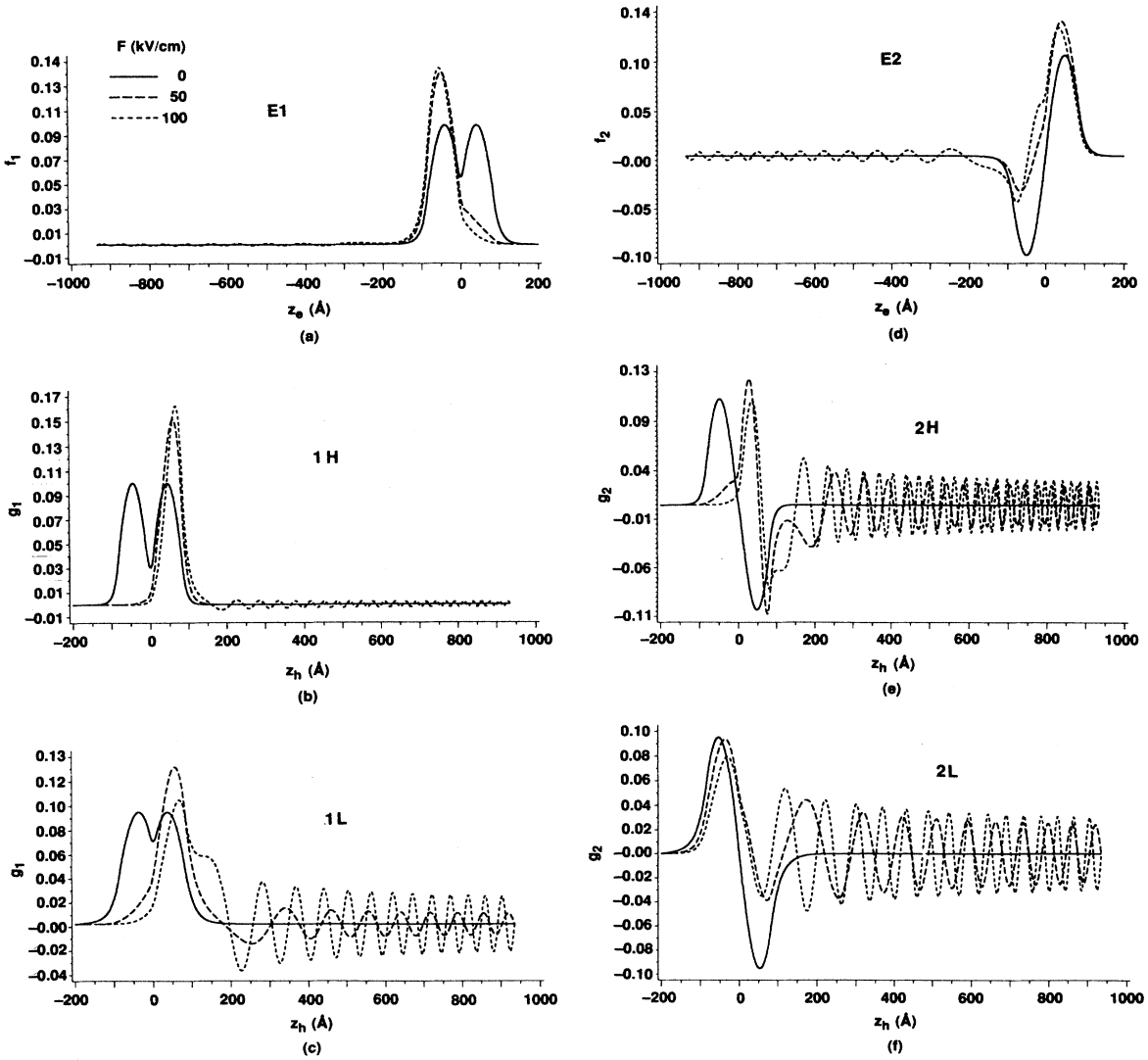


FIG. 6. With $\delta=0$, the envelope functions with various fields for electrons (a) [(d)], heavy holes (b) [(e)], and light holes (c) [(f)] in the ground state (first-excited) state. $F=0$ (solid curves), 50 kV/cm (long bars), and 100 kV/cm (short bars).

first-excited state because of its higher energies.

Oscillator strengths as a function of $F$ are plotted in Figs. 7(a) and 7(b) for allowed and forbidden transitions, respectively. Figure 7(a) [7(b)] shows that for the allowed (forbidden) transitions, when $F$ increases, oscillator strengths decrease (increase) in the low-field region. Among forbidden transitions, $O_{21\mathrm{H}}$ may become the dominant transition in the high-field region ($F \sim 100$ kV/cm). The variations of the total energies $E^{\mathrm{tot}}_{nm\mathrm{H}(nm\mathrm{L})}$ [Eq. (24)] with the field $F$ for allowed and forbidden transitions are shown in Figs. 7(c) and 7(d), respectively.

### C. Asymmetric wells with electrical fields ($F \neq 0$, $\delta \neq 0$)

We take $\delta = 10$ Å and $-10$ Å as examples to illustrate the consequences of the asymmetries of the double-quantum-well structures. If $\delta$ equals 10 Å ($-10$ Å), $W_1$ equals 85 Å (65 Å) and $W_2$ equals 65 Å (85 Å), i.e., the left well becomes thicker (thinner). We assume that the electrical field is along the $z_{e,h}$ axis. The envelope functions $f_2(z_e)$ for the electron in the first-excited state are chosen as examples, and shown in Figs. 8(a) and 8(b) for $\delta = 10$ Å and $-10$ Å, respectively. When $F$ is 0 kV/cm, Fig. 8(a) [8(b)] shows that more electrons populate the right (left) well. As $F$ increases, electrons begin to redistribute themselves. When $F$ is 100 kV/cm, we see that the possibility of an electron leaking out of the CDQW and residing in the left-barrier region is larger (smaller) if $\delta$ is 10 Å ($-10$ Å), as shown in Fig. 8(a) [8(b)]. Therefore, from comparison of Fig. 6(d) with Figs. 8(a) and 8(b), we expect to see significant changes in $E^{\mathrm{tot}}_{nm\mathrm{H}(nm\mathrm{L})}$ and $O_{nm\mathrm{H}(nm\mathrm{L})}$ as functions of $F$. We summarize all these variations in the absorption spectra in Figs. 9(a), 9(b), and 9(c) with $\delta = 10$, 0, and $-10$ Å, respectively. We find that (1) with $F = 0$ kV/cm only absorption peaks due to allowed transitions are present in the spectra since the oscillator strengths for forbidden transitions are too small to be significant in the absorption even when $\delta \neq 0$, as shown in Fig. 4; (2) with increasing $F$, absorption peaks due to allowed transitions quickly disappear and absorption peaks due to forbidden transitions are observed in the spectra. Note that when $F \neq 0$ and if (1) $\delta = 10$ Å, there are two dominant absorption peaks: the 12H peak on the lower-energy side and the 21H peak superimposed with the 12L peak to produce a strong absorption line on the higher-energy side; (2) with $\delta = -10$ Å, only one dominant peak, 21H, appears on the lower-energy side and weaker peaks 21L and 22H appear in the higher-energy side. Here, we conclude that, by shifting the central barrier to the right-hand side or to the left-hand side of the double quantum well (see Fig. 1), the absorption spectra as a function of $F$ are varied drastically not only in the line shapes but also in the peak locations of the energy spectra.

### D. Comparison with experimental results

In applying the model developed above to calculate absorption spectra as a function of applied electric field to a specific structure which has been studied experimentally

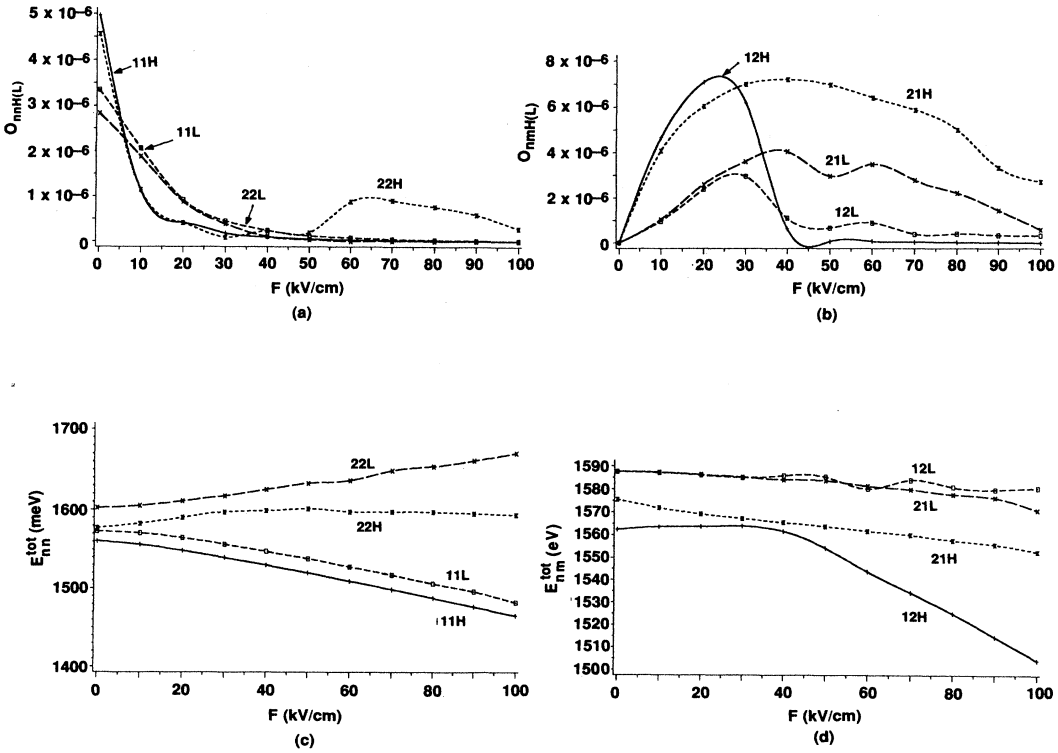


FIG. 7. With $\delta = 0$, the oscillator strengths and the total energies are plotted as a function of fields $F$ for allowed transitions (a) and (c) and for forbidden transitions (b) and (d), respectively.

previously,[20] we found that the best agreement between calculated exciton energies and oscillator strengths and experimentally derived results was obtained using a set of structural parameters slightly different from the nominal values given earlier.[20] The new set of quantum-well widths is consistent with our latest results on single-QW exciton energies whose widths were obtained directly by monitoring reflection high-energy electron-diffraction oscillations.[24] The new set of input parameters is $Ga_{1-x}Al_xAs/GaAs$ with $x=0.29$, $V_e=247.1$ meV, $V_h=119$ meV, $D_1=D_2=850$ Å, $W_1=W_2=64$ Å, $B=15$ Å, $m_e^*=0.0665$, $m_H^*=0.34$, and $m_L^*=0.105$ for the masses in the well regions, $m_{e'}^*=0.0904$, $m_{H'}^*=0.36$, and $m_{L'}^*=0.13$ for the masses in the barrier regions, $\kappa=12.2$, and $E_g=1519$ meV.

The experimental photoluminescence excitation (PLE) spectra as a function of electric field $F$ are given in the left-hand column [Figs. 10(a)–10(d)], while the calculated absorption spectra are presented in the right-hand column [Figs. 10(e)–10(h)]. The correspondence with the notation of Ref. 20 is 11H=1, 22H=3, 11L=6, 22L=8, 12H=2, 21H=5, 12L=4, and 21L=7. It is important to realize that while PLE spectra are analogous to absorption spectra, they are not identical. Therefore, exact agreement of the calculated results and the PLE spectra is not expected. However, it is reasonable to assume that when strong (weak) peaks are present in absorption spectra, they will also be present in PLE spectra. This is clearly evident in Fig. 10 for several different values of electric field. The calculated and experimental exciton energies $(E_{nm\mathrm{H}(nm\mathrm{L})}^{\mathrm{tot}}-E_g)$ as a function of $F$ are shown in Figs. 11(a) and 11(b) for the allowed transitions and forbidden transitions, respectively. The conversion from experimental measured voltage to internal electric field was accomplished by assuming that the total net voltage (applied minus built-in) occurred across the undoped region in the structure. For allowed transitions, calculated curves are in excellent agreement with experiment [Fig. 11(a)], but for forbidden transitions the agreement is less satisfactory, particularly for the 12H and the 12L transitions. This may be a consequence of the fact that band nonparabolicities and light- and heavy-hole mixing were omitted in the calculations.

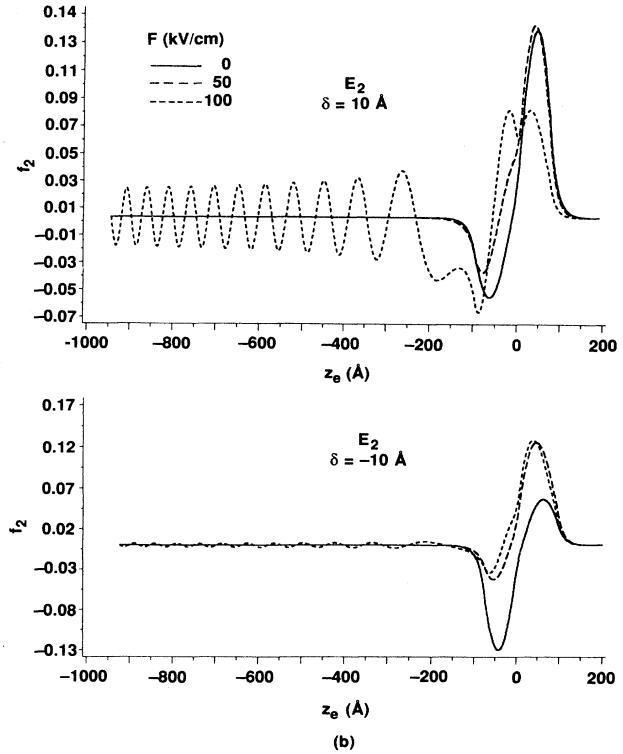


FIG. 8. The envelope functions for the electron in the first-excited state with (a) $\delta=10$ Å and (b) $\delta=-10$ Å under three electric fields. $F=0$ (solid curves), 50 kV/cm (long bars), and 100 kV/cm (short bars).

## IV. SUMMARY

We have studied the excitonic spectra of asymmetric coupled double quantum wells in external electric fields using a two-band model in the effective-mass envelope-function approximation. The confined parts of the total Hamiltonian for the electron and hole, with the external

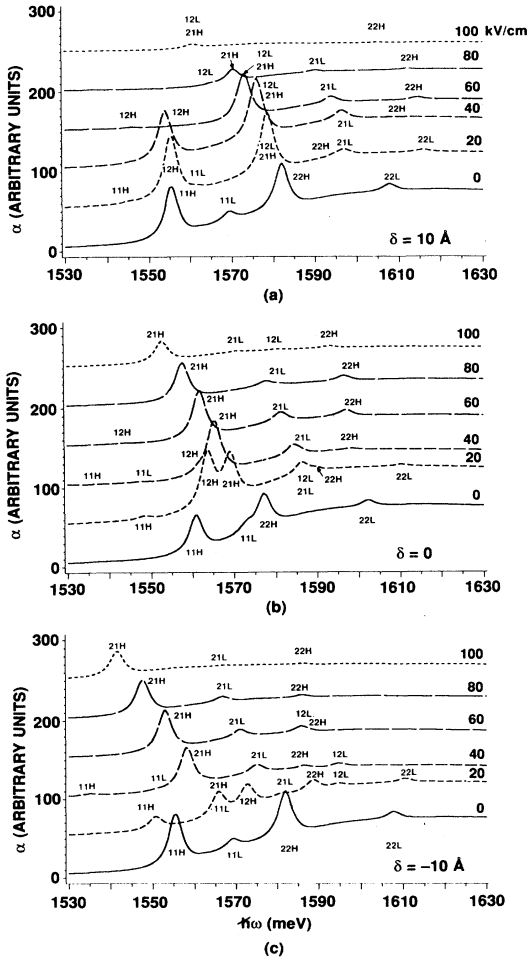


FIG. 9. The absorption spectra of the CDQW are plotted with various electric fields for (a) $\delta=10$ Å, (b) $\delta=0$, and (c) $\delta=-10$ Å.

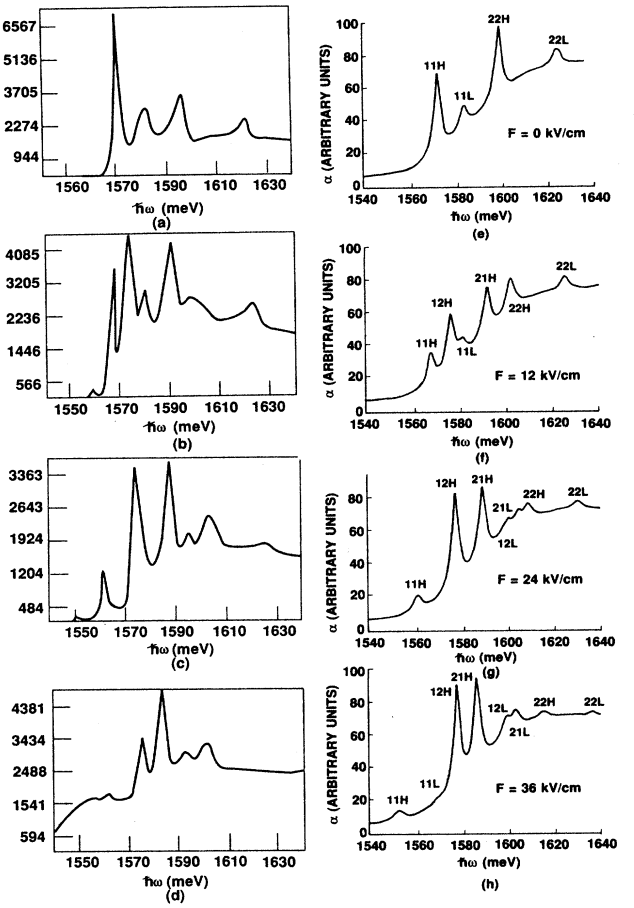


FIG. 10. The experimental PLE spectra (left-hand column) compared with the calculated absorption spectra (right-hand column) for various fields. $F=0$, 12, 24, and 36 kV/cm.

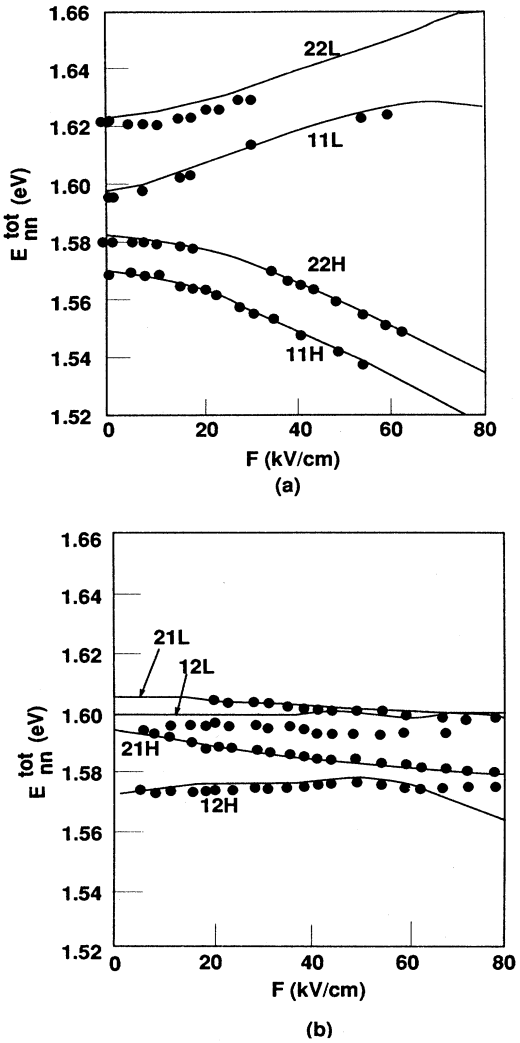


FIG. 11. The total energies of (a) allowed transitions and (b) forbidden transitions vs electric fields $F$. Theory (solid curves) and experiment (dots).

electrical field included, were solved numerically in order to obtain exact eigenenergies and eigenfunctions. Only bound states exist because we have assumed infinite potential wells at both ends of the CDQW structure. A hydrogenlike Schrödinger equation was derived to describe the excitonic effects and was solved variationally for the $1s$ state. The absorption spectra were obtained by using the dipole approximation for the excitonic and the continuum contributions. The line shapes were assumed to be Lorentzian. We examined variations of the envelope functions, eigenenergies, oscillator strengths, and absorption spectra with the fields for symmetric and asymmetric wells. We found that, without electric fields, asymmetries of the CDQW structure can yield nonzero oscillator strengths for "forbidden" transitions, but these are too small (about 1 order of magnitude less than the oscillator strengths of "allowed" transitions) to be important in the absorption spectra. Also, we found that with increasing electric fields, asymmetries of the CDQW structure can yield entirely different absorption spectra, depending on the shifts of the central barrier towards the right- or left-hand sides of the well. We compared our theoretical calculations with the experimental results on the absorption spectra and the locations of the exciton peaks in energy, and were able to reach good agreement if we chose the parameters of the CDQW appropriately. In conclusion, it is important to point out that while QW widths for single wells can be determined relatively straightforwardly by using energies of quantum well excitons, widths of coupled double wells are more difficult to obtain. However, from the good agreement between experiment and theory demonstrated in this work, it appears that the model developed here can yield accurate results.

## APPENDIX: NUMERICAL SCHEME FOR Eq. (6)

It is well known that the Runge-Kutta method can be used to solve simultaneous first-order and, hence, higher-order ordinary differential equations. When combined, Eqs. (2) and (6) become

$$-\partial_z \frac{1}{m^*(z)} \partial_z \psi_{(z)} + [V(z)+F(z)-E]\psi(z)=0 ,$$

where all subscripts have been omitted in the original equations, and $m^*(z)$ and $V(z)$ are constants in various regions 1–5, as indicated in Fig. 1. In region 1, we have

$$\frac{1}{m'}\partial_z^2\psi+[V+F(z)-E]\psi=0 ,$$

and we identify $\psi\rightarrow Y_1$ and $\partial_z\psi\rightarrow Y_2$. Then, Eq. (A2) can be cast as

$$Y_1'=Y_2 \tag{A1}$$

and

$$Y_2'=M'(V+F_z-E)Y_1 , \tag{A2}$$

where the prime represents $\partial z$. The physical quantities needed for calculating the absorption coefficient and for Eq. (13) are

$$Y_3=\int dz\, Y_1^2 \quad \text{for normalization} ,$$

$$Y_4=\int dz\, zY_1^2 \quad \text{for average } z ,$$

and

$$Y_5=\int dz\, z^2Y_2^2 \quad \text{for average } z^2 .$$

Thus, we have

$$Y_3'=Y_1^2 , \tag{A3}$$

$$Y_4'=zY_1^2 , \tag{A4}$$

$$Y_5'=z^2Y_1^2 . \tag{A5}$$

In order to save computing time for faster convergence, we perform the following analysis. One of the initial conditions at $z=z_L=-B/2-W_1-D_1$ is given by Eq. (7) as

$$Y_1(z_L)=0 . \tag{A6}$$

We know that the general solution for Eqs. (A1) and (A2) is a linear combination of Airy functions, $\mathrm{Ai}(x)$ and $\mathrm{Bi}(x)$. Thus, we write

$$Y_1(z)=C_1\,\mathrm{Ai}(\xi)+C_2\,\mathrm{Bi}(\xi) ,$$

where

$$\xi=(m'F)^{1/3}\left[z-\frac{E-V}{F}\right]$$

with $F>0$ assumed. After differentiating $Y_1(z)$ with respect to $z$ and combining with Eq. (A6), $Y_1'(z_L)=Y_2(z_L)$ has the simple form written as

$$Y_2=\mathrm{Bi}^{-1}[\xi(z=z_L)] . \tag{A7}$$

For a given set of input data ($m'$, $V$, $F$, $E$), Eq. (A7) gives the exact slope of $\psi(z)$. The other initial conditions are

$$Y_3(z_L)=Y_4(z_L)=Y_5(z_L)=0 \tag{A8}$$

because of $Y_1(z_L)=0$. The first-order differential equations (A1)–(A5) are solved simultaneously with conditions (A6)–(A8) and terminated at $z=z_L'=B/2-W_1$. This completes the calculations in region 1.

In region 2, we replace $m'\rightarrow m$ and $V\rightarrow 0$ in Eq. (A2) and set $Y_iz_L'=Y_i(z_L)$ for $i=1$–5, except $i=2$, which needs special care. To ensure the continuity of the particle flux, $Y_2(z)$ [i.e., $y'(z)$] requires

$$Y_2(z_L')=m'Y_2(z_L)/m .$$

Then, Eqs. (A1)–(A5) with initial conditions discussed above are solved for region 2. Similar numerical procedures are performed for regions 3, 4, and 5. The boundary at the right-hand side is $z=z_R=B/2+W_2+D_2$. For a given set of input data ($m'$, $V$, $F$, $E$), we examine $Y_1(z_R)$ iteratively until it converges to a desired small positive quantity $\lambda$. If $Y_1(z_R)$ has not converged to $\lambda$, we choose a new value of $E$ until the criterion $|Y_1(z_R)|\le\lambda$ is satisfied. This completes the eigenvalue problem for the electron in the conduction band. A more efficient way to complete the computing is to use the fact that when $z\rightarrow+\infty$, and $F\neq 0$, $Y_1(z)$ must converge to $C\,\mathrm{Ai}(x)$ where $C$ is a constant. Thus, we evaluate the absolute value of a quantity

$$Y_1(z)/Y_2(z)-\mathrm{Ai}(\xi)/m'F)^{1/3}\,\mathrm{Ai}'(\xi)=\eta .$$

When $\eta$ converges to $\lambda$ as desired at $z=z'\le z_R$, the computation is ended.


[1]D. F. Blossey and P. Handler, in *Semiconductors and Semimetals*, edited by R. K. Willardson and A. C. Beer (Academic, New York, 1972), Vol. 9, p. 257, and references therein.

[2]G. E. Stillman, C. M. Wolfe, C. O. Bozler, and J. A. Rossi, Appl. Phys. Lett. **28**, 544 (1976).

[3]R. H. Kingston, B. E. Burke, K. B. Nichols, and F. J. Leonberger, Appl. Phys. Lett. **41**, 413 (1982).

[4]D. F. Blossey, Phys. Rev. B **2**, 3976 (1970).

[5]J. D. Dow and D. Redfield, Phys. Rev. B **1**, 3358 (1970).

[6]D. S. Chemla, D. A. B. Miller, and P. W. Smith, Opt. Eng. **24**, 556 (1985).

[7]T. H. Wood, Appl. Phys. Lett. **48**, 1413 (1986).

[8]T. H. Wood, C. A. Burrus, D. A. B. Miller, D. S. Chemla, T. C. Damen, A. Gorssard, and W. Wiegmann, Appl. Phys. Lett. **44**, 16 (1984).

[9]G. Bastard, E. E. Mendez, L. L. Chang, and L. Esaki, Phys. Rev. B **28**, 3241 (1983).

[10]D. A. B. Miller, D. S. Chemla, T. C. Damen, A. C. Gossard, W. Weigmann, T. H. Wood, and C. A. Burrus, Phys. Rev. B **32**, 1043 (1985).

[11]F. M. Fernandez and E. A. Castro, Physica A **84**, 421 (1976).

[12]E. J. Austin and M. Jaros, Phys. Rev. B **31**, 5569 (1985).

[13]Z. Ikonic, V. Milanovic, and D. Tjapkin, J. Phys. C **20**, 1147 (1987).

[14]G. D. Sanders and K. K. Bajaj, Phys. Rev. B **35**, 2308 (1987), and references therein.

[15]E. J. Austin and M. Jaros, J. Phys. C **19**, 533 (1986).

[16]H. Kawai, J. Kaneko, and N. Watanabe, J. Appl. Phys. **58**, 1263 (1985).

[17]A. Yariv, C. Lindsey, and U. Sivan, J. Appl. Phys. **58**, 3669

(1985).
[18]H. Q. Le, J. J. Zayhowski, and W. D. Goodhue, Appl. Phys. Lett. **50**, 1518 (1987).
[19]S. R. Andrews, C. M. Murray, R. A. Davies, and T. M. Kerr, Phys. Rev. B **37**, 8198 (1988).
[20]Y. J. Chen, E. S. Koteles, B. S. Elman, and C. A. Armiento, Phys. Rev. B **36**, 4562 (1987).
[21]M. N. Islam, R. L. Hillman, D. A. B. Miller, D. S. Chemla, A. C. Gossard, and J. H. English, Appl. Phys. Lett. **50**, 1098 (1987).
[22]M. Shinada and S. Sugano, J. Phys. Soc. Jpn. **21**, 1396 (1966).
[23]F. Bassani and G. Parravicini, *Electronic States and Optical Transitions in Solids* (Pergamon, Oxford, 1975), Chap. 5.
[24]B. Elman and E. S. Koteles (private communication).